



Published in final edited form as:

*Neuroimage*. 2008 April 15; 40(3): 1034–1043.

## Action potential propagation imaged with high temporal resolution near-infrared video microscopy and polarized light

Jennifer L. Schei<sup>1</sup>, Matthew D. McCluskey<sup>1</sup>, Amanda J. Foust<sup>2</sup>, Xin-Cheng Yao<sup>3</sup>, and David M. Rector<sup>2,\*</sup>

<sup>1</sup>*Department of Physics and Astronomy, Washington State University, Pullman, WA 99164-2814.*

<sup>2</sup>*Department of Veterinary and Comparative Anatomy, Pharmacology, and Physiology, Washington State University, Pullman, WA 99164-6520.*

<sup>3</sup>*Department of Biomedical Engineering, University of Alabama, Birmingham, AL 35294-2182*

### Abstract

To identify the neural constituents responsible for generating polarized light changes, we created spatially resolved movies of propagating action potentials from stimulated lobster leg nerves using both reflection and transmission imaging modalities. Changes in light polarization are associated with membrane depolarization and provide sub-millisecond temporal resolution. Typically, signals are detected using light transmitted through tissue; however, because we eventually would like to apply polarization techniques in-vivo, reflected light is required. In transmission mode, the optical signal was largest throughout the center of the nerve, suggesting that most of the optical signal arose from the inner nerve bundle. In reflection mode, polarization changes were largest near the edges, suggesting that most of the optical signal arose from the outer sheath. In support of these observations, an optical model of the tissue showed that the outer sheath is more reflective while the inner nerve bundle is more transmissive. In order to apply these techniques in-vivo, we must consider that brain tissue does not have a regular orientation of processes as in the lobster nerve. We tested the effect of randomizing cell orientation by tying the nerve in an overhand knot prior to imaging, producing polarization changes that can be imaged even without regular cell orientations.

### Introduction

Several mechanisms are responsible for fast optical changes in the intensity, polarization, and scattering from neural tissue. Birefringent materials exhibit different refractive indices along perpendicular axes causing linearly polarized light oriented off-axis to split into two components with different polar angles. Biological materials can alter light polarization through several physical processes including birefringence, light scattering polarization changes, and absorption of light with specific polar angles (dichroism). The activation of sodium channels induces a reorientation of the peptide bonds, thereby altering the polarization of scattered light (Landowne 1985). Studies of isolated lobster nerves have suggested that polarized light is also affected by changes in the cylindrical shape of the nerve fibers (Cohen et al., 1968; Yao et al., 2005a). Axonal swelling that occurs during neural activation, caused by the influx of water, may lead to a change in polarized light (Tasaki and Byrne 1993; Yao

\*Corresponding Author: David M. Rector PhD. Associate Professor, Department VCAPP, Washington State University, 205 Wegner Hall, Pullman, WA 99164-6520, Phone: 509.335.1587, Fax: 509.335.4650, Email: drector@vetmed.wsu.edu

**Publisher's Disclaimer:** This is a PDF file of an unedited manuscript that has been accepted for publication. As a service to our customers we are providing this early version of the manuscript. The manuscript will undergo copyediting, typesetting, and review of the resulting proof before it is published in its final citable form. Please note that during the production process errors may be discovered which could affect the content, and all legal disclaimers that apply to the journal pertain.

et al., 2005a; Foust and Rector, 2005). The additional water also increases the transparency of the nerve fibers, which reduces the scattered light intensity.

In principle, if it were possible to detect only those photons that were altered by neural activation, then the optical signal would be highly sensitive to tissue activity. In practice, however, most of the light is multiply scattered and is not specific to changes in neural activity. The resulting changes in the overall light intensity are on the order of  $10^{-5}$  for large angle scattering (Cohen et al., 1968; Carter et al., 2004). By isolating specific biophysical properties of scattered light within nerves, it should be possible to optimize the optical detection of neural activation (Foust et al., 2007). For example, changes in polarized light are more sensitive to neural activity by an order of magnitude ( $10^{-4}$ ) because the cross polarizers reject more background light that is unaltered by neural changes. Additionally, optical coherence tomography (OCT) techniques could be used to exclude non-specific light (Uma Maheswari et al., 2003; Yao et al, 2005b).

The lobster nerve is an excellent model system for imaging neural activity, allowing for relatively simple experiments and data interpretation. Since light passed through crossed polarizers excludes some of the non-specific light from the neural tissue and increases the changes in the fast optical signals compared to scattering signals, we focused the current experiments on detecting changes in polarization. Optical signals from lobster nerves are best detected with light-emitting diodes (LEDs) and photodiode detectors (Foust et al., 2005). In the present work, we used a superluminescent diode (SLD), which has similar characteristics of LEDs with the high intensity of lasers, and a charge-coupled device (CCD) imaging array to obtain spatially resolved images of polarized light transmitted and reflected from a stimulated lobster nerve. We compared transmitted and reflected light modalities to characterize the optical properties of the materials comprising the lobster nerve and determine the spatial components from which dominating signals arose.

Using visible and near-infrared photons to image the human brain shows promise in providing a noninvasive means for mapping neural activity. Current functional imaging techniques are sensitive to changes in light absorption caused by hemodynamic phenomena. In these measurements, neural activation results in increased metabolism, a corresponding increase in blood flow, and increased oxy-hemoglobin concentration that can be detected optically in invasive (e.g. Haglund et al., 1992; Grinvald 1992) and noninvasive (e.g. Chance et al., 1997; Hoshi et al., 2000) experiments. While functional metabolic imaging can provide relatively good spatial resolution ( $< 1$  mm invasively and  $\sim 1$  cm noninvasively), the time scales are on the order of hundreds of milliseconds to seconds, much slower than the “fast” optical changes that are correlated with the membrane potential (Cohen et al., 1968; Cohen et al., 1972; Landowne 1985; Rector et al., 2005). We are interested in eventually imaging these fast events in-vivo to improve the temporal resolution and provide signals that correspond more closely to electrical activation.

We used isolated lobster nerves because they produce very little physiological noise and the cells are oriented in the same direction. These favorable conditions, however, are not ideal when employing these imaging techniques in-vivo because the tissue is predominantly composed of randomly oriented fibers. If polarization sensitive signals could be detected within neural tissue, which has randomly oriented fibers, then these techniques could greatly reduce the background noise and allow for extraction of more sensitive fast optical signals. We tested our imaging techniques with random cell orientation by tying the nerve in an overhand knot before imaging. We propose that a better understanding of the depolarizing properties of neural tissue will lead to the development of novel optical brain imaging technologies.

## Methods

Nerves from the first and second lobster legs, *Homarus americanus* (Sea View Lobster, Kittery, ME, USA), were used to compare the reflected and transmitted polarization signals. Each nerve, approximately 6 cm long and 1-2 mm in diameter, was extracted using the Furusawa pulling out method (Furusawa, 1929) and sutured on each end. We then placed the nerve in a sample chamber (Figure 1) brimmed with a bath solution (525 mM NaCl, 13.3 mM KCl, 12.4 mM CaCl, 24.8 mM MgCl, and 5 mM dextrose). The center of the sample chamber contained a glass microscope slide which permitted light to transmit through the nerve. In reflection mode imaging, we placed another glass microscope slide over the top of the imaging area to reduce reflections caused by the bath solution meniscus. Each side of the imaged area contained 4 wells fitted with silver electrodes. We isolated each well using petroleum jelly before flooding the sample chamber with the bath solution. One end of the nerve was stimulated by a pair of electrodes delivering a 2mA current pulse at a width of 0.2 ms using a direct current isolated stimulator (Model A365R, World Precision Instruments, Inc., Sarasota, FL, USA). Stimulus intervals were randomly administered between 1 and 2 seconds. Population action potentials were measured both before and after the imaging window using two pairs of electrodes which were spaced 21 mm apart. The signal was averaged over 200 stimuli for each nerve.

A schematic diagram of the transmission mode experimental setup is shown starting from the bottom in Figure 2. We used a free-space SLD module (SLD-380-MP3-TOW2-PD, Superlum Diodes Ltd., Moscow, Russia), with a peak emission wavelength of 833 nm and spectral bandwidth of 23 nm, to illuminate the nerve. The beam was collimated by a lens with a focal length of  $f = 5$  mm (06 3008, Linos Photonics, Milford, MA, USA) and polarized (46087, Edmund Optics, Barrington, NJ, USA) 45 degrees with respect to the nerve. The light projected through the image window of the sample chamber and illuminated the nerve with a 2-3 mm diameter spot. A second polarizer (46087, Edmund Optics, Barrington, NJ, USA) transmitted crossed-polarized light. We focused the image using a lens of focal point  $f = 12.5$  mm (06 3032, Linos Photonics, Milford, MA, USA) onto the CCD camera chip (TC255, Texas Instruments, Dallas, TX, USA) with 10 micron square pixels. Custom built control and acquisition systems were used to collect images at a rate of 1667 Hz (Rector et al., 2003).

In the reflection mode experimental setup, starting from the left in Figure 2, we used the same near-infrared SLD light module, a lens of focal length  $f = 5$  mm to collimate the SLD light, and a polarizer to reject  $p$ -polarized light and transmit  $s$ -polarized light (in the geometry of this experiment,  $s$ -polarized light was parallel to the optical table). The  $s$ -polarized light was reflected onto the nerve bundle, which yielded an illumination diameter of 2-3 mm, using a polarizing beam splitter (G335599000, Linos Photonics, Milford, MA, USA). Light scattered off of the nerve and traveled through the polarizing beam splitter that only transmitted  $p$ -polarized light (Yao et al., 2005a). We focused the light with the same lens ( $f = 12.5$  mm) onto the CCD that acquired images at a rate of 1667 Hz.

The long axis of the nerve and the CCD array were oriented at a 45° angle to the polarization of the light in order to maximize the response (Cohen et al., 1968; Yao et al., 2005a). The image of the nerve fell on a 108 x 162 pixel portion of the CCD. In order to integrate all of the available light and reduce noise, every 2 pixels were horizontally binned and every 9 pixels were vertically binned, resulting in a 54 X 18 pixel image.

All data was analyzed using Octave ([www.octave.org](http://www.octave.org)), an open source data analysis and mathematical modeling package. We measured the propagation velocity of the electrical signals by dividing the distance between the two electrode pairs (21 mm) by the difference in the time from the population action potential peaks between the first pair of electrodes, before the imaging window, and the second pair of electrodes, after the imaging window. The

integrated polarization signal was obtained by averaging the signal across all pixels in the image and dividing by the baseline intensity ( $dI/I$ ). We calculated the signal to noise ratio (SNR) by dividing the peak amplitude of the signal by the root mean square (RMS) of the data from 150-500 ms. RMS values were read in analog to digital conversion units from the digitizer and are reported in arbitrary units (AU).

The raw image of the nerve was produced by averaging the temporal component of the signal for each pixel in the image and plotting the signal amplitudes. The spatially resolved color images are plots of the signal amplitude given by

$$A(x, y) = - \sum_t f(x, y, t), \quad (1)$$

where  $f(x, y, t)$  was the baseline-corrected signal for pixel  $(x, y)$  at a time  $t$ . The negative sign was used so that  $A$  was positive when the response *decreases*. The maximal signal amplitude was calculated by summing each pixel across the time interval  $t = 18-55$  ms, corresponding to the time window where the response was maximal.

Since our signal to noise ratio was about 3:1 for individual pixels, we needed a fitting algorithm to model and accurately determine the time dependence of the signal for each pixel. We used the following impulse response function to model the signal:

$$F(x, y, t) = \begin{cases} \frac{A(x, y)}{\tau^2} (t - t_0) e^{-\frac{(t-t_0)}{\tau}} & t \geq t_0 \\ 0 & t < t_0 \end{cases}, \quad (2)$$

where  $F(x, y, t)$  was the response function;  $A(x, y)$  was the signal amplitude from Equation 1;  $t$  was the time;  $\tau$  and  $t_0$  were adjustable constants. This function describes a linear response starting at  $t_0$ , followed by an exponential decay. The time  $t_0$  was determined for each pixel using the method of least squares. The rise time  $\tau$  was assumed to be the same for all pixels; a value of  $\tau = 0.004$  s was found to yield the best fit.

In order to determine the relative amounts of polarization changes emanating from different parts of the nerve, pixels from the intensity amplitude plots were averaged horizontally, along the length of the nerve, and divided by the average signal baseline intensity. The resulting plot was the signal  $dI/I$  versus vertical pixel number where one pixel equals 0.28 mm. We averaged multiple nerves together to further separate the signal from the noise. Each plot was stretched across a set number of pixels to compensate for variations in nerve positions and widths. The signal amplitudes were also normalized to one in order to account for varying overall intensities in each image. We used 22 nerves total, 19 in transmission mode and 3 in reflection mode.

We quantified the relative contributions of reflected and transmitted light to the overall signal by developing a model of the intensity profile across the width of the nerve using simple geometric considerations. The nerve was modeled as a cylindrical nerve bundle with a radius  $R_b$  surrounded by a sheath membrane of thickness  $R_s$  (Figure 3) to determine the optical properties of the comprising materials. Light rays were incident on the nerve at a perpendicular distance  $r$  from the center and the depolarization of light was assumed to be proportional to the path length through the material. On average, we assumed that photons traveled to the center of the nerve before being scattered. We calculated the path length through each material using the Pythagorean theorem. The path length through the outer sheath,  $d_s$ , as a function of  $r$  was given by the following equation:

$$d_s(r) = \begin{cases} 0 & r > R_s + R_b \\ \sqrt{(R_s + R_b)^2 - r^2} & R_b < r < R_b + R_s \\ \sqrt{(R_s + R_b)^2 - r^2} - \sqrt{R_b^2 - r^2} & r < R_b \end{cases}. \quad (3)$$

When  $r$  was greater than  $R_b$  and less than  $R_b + R_s$ , light traveled through the outer sheath only whereas when  $r$  was less than  $R_b$ , light traveled through both the outer sheath and the inner bundle. The path length through the inner bundle was calculated using the following equation:

$$d_b(r) = \begin{cases} 0 & r > R_s + R_b \\ \sqrt{R_b^2 - r^2} & r < R_s + R_b \end{cases}. \quad (4)$$

The polarization properties of each material was modeled separately using  $(A_s d_s(r) + A_b d_b(r))$  where  $d_s$  and  $d_b$  were the path lengths through the outer sheath and inner bundle, respectively, as calculated in Equation 3 and Equation 4;  $A_s$  and  $A_b$  were empirical constants. We modeled the intensity of light traveling through a medium using an exponential. We assumed a weak scattering limit meaning that photons underwent few scattering events before detection. In transmission mode, the intensity of the light was modeled by:

$$I_T(r) = I_0 e^{-(k_s d_s + k_b d_b)}, \quad (5)$$

where  $I_0$  was the initial intensity;  $k_s$  and  $k_b$  were the extinction coefficients of the outer sheath and inner bundle, respectively;  $d_s$  and  $d_b$  were the path lengths through the respective materials. Photons were assumed to scatter elastically. In other words, the light could only be either transmitted or reflected through the material. From this premise, the intensity of reflected light was given by:

$$I_R(r) = I_0 \left(1 - e^{-(k_s d_s + k_b d_b)}\right). \quad (6)$$

By combining the polarization properties of the material with the intensity of the signal, we modeled the transmission mode signal using the equation:

$$S(r) = (A_s d_s(r) + A_b d_b(r)) e^{-(k_s d_s + k_b d_b)}, \quad (7)$$

where  $S(r)$  was the optical signal obtained from the nerve at each point along the radius;  $d_s$  and  $d_b$  were the path lengths through the membrane and bundle, respectively;  $A_s$  and  $A_b$  were empirical constants;  $k_s$  and  $k_b$  were the extinction coefficients of the material. The reflection mode signal was modeled using the equation:

$$S(r) = (A_s d_s(r) + A_b d_b(r)) \left(1 - e^{-(k_s d_s + k_b d_b)}\right). \quad (8)$$

Equation 7 and Equation 8 were numerically integrated over each pixel width to simulate the CCD response. The parameters were determined using a reduced chi-square fit.

An action potential movie was created by baseline correcting, temporally smoothing the signal by a factor of 10 using a convolution smoothing function, and spatially smoothing each pixel using a  $3 \times 3$  spatial convolution function. Each frame was subtracted from a baseline generated by averaging the first 10 frames together and divided by the DC light intensity, resulting in  $dI/I$ . To demonstrate the left to right propagation of the action potential, the image of the nerve was divided into three regions where the middle region was twice the length of the two outer regions. The optical signal from the outer two regions was divided by the baseline intensity to give  $dI/I$ . The signal was filtered between 0 and 200 Hz and numerically differentiated to illustrate the latency of the signal between the two ends of the nerve. We expect that the leftmost region will change before the rightmost region if the action potential propagates from left to right.

In order to test the effect of random cell orientation, as occurs in-vivo, we collected data from 5 nerves, each tied in an overhand knot before imaging. We created images of the average response over time to show the locations of the polarization signal. The temporal signal was filtered between 0 and 400 Hz, smoothed by a factor of 2, and then plotted for four individual regions within the nerve. An overlying fit to the signal was then obtained using Equation 4.

### 3. Results and Discussion

#### Simultaneous Electrical and Polarization Signals

A plot of the change in intensity divided by the baseline intensity ( $dI/I$ ) integrated over the entire imaged region for both reflection and transmission mode along with the electrophysiological response (EPR) is shown in Figure 4. The EPR signal (top panel of Figure 4) was recorded both before and after the imaging window, as shown in Figure 1 (ii and iii, 21 mm apart), and both responses are composed of several waveforms corresponding to the activation of axon populations of different sizes (Carter et al., 2004). Propagation velocities were calculated for the different axon sizes using the EPR signals. For large (l), medium (m), and small (s) axons, the calculated velocities were 3.28 m/s, 2.04 m/s, 1.63 m/s respectively. The polarization changes in both reflection and transmission mode (bottom panel of Figure 4) shows a clear response after electrical stimulation, corresponding to the timing of the EPR. While the signal is discernible in both transmission and reflection mode imaging, the signal amplitude in transmission mode was about 3 times larger than in reflection mode. Since the total noise for the recorded signals was 12.3 AU (arbitrary units), and the measured RMS noise for the recording system was 9.1 AU, system noise accounted for a larger proportion of the RMS noise calculated due to physiological noise (8.3 AU). Thus, a significant source of noise in this data originated from the CCD camera. A lower noise camera should greatly improve these measurements. The SNR in transmission mode is 5.6 while the SNR in reflection mode is 3.6. The low signal amplitude in reflection mode may be due to significantly fewer photons both changing polarization and scattering a full 180 degrees. In transmission mode, a larger number of photons change polarization due to neural activity and transmit directly through the material with few scattering events. Additionally, in reflection mode, some scattering from interfaces may not have been specific to neural activity, causing a weaker signal.

#### Transmission Mode Imaging

Spatially resolved images in transmission mode are shown in Figure 5(A & B). The horizontal and vertical coordinates are parallel and perpendicular to the nerve respectively. Figure 5(A) is the transmitted light intensity image of the nerve averaged across time. The diffuse properties of the nerve bundle required a lens to focus the light onto the camera. Reduced spatial resolution and blurring of the image was partially dependent on our ability to adjust the focus of the image as well as pixel binning across the image. The image of the nerve is vertically centered in the plot, as indicated by the two arrows. The intensity of the light appears evenly spread throughout the nerve. A spatial plot of the signal amplitude, which is summed over the peak of the response (18-55 ms), is shown in Figure 5(B). An increase in amplitude correlates to a decrease in intensity pseudo-colored with warmer colors. The large changes in birefringent light appear ubiquitously throughout the nerve.

#### Reflection Mode Imaging

A spatially resolved reflection mode intensity image averaged across time is shown in Figure 5(C). The edges of the nerve bundle are clearly resolved in this picture, as indicated by the arrows. Some of the scattered light, particularly near the center of the image, may be due to reflections from the glass/water interface. A spatial plot of the signal response, summed from 18 to 55 ms, is shown in Figure 5(D) where a decrease in intensity corresponds to warmer colors. The highest intensity of light occurred at the edges of the nerve (Figure 5D). This suggests that a significant fraction of the reflected polarization changes in lobster nerves arose from the outer fascicle sheath.

## Temporal Signal Components

We modeled the temporally resolved polarization signal in order to extract the neural components from the noise. This model can serve as a template for noisy reflection mode signals and perhaps be used in single pass trials. Figure 6 shows the signal for four separate regions (a, b, c, and d) corresponding to the locations outlined in Figure 5. The corresponding temporal model was fit using Equation 2.

The action potential propagates along the nerve from left to right in Figure 5(D). In principle, this motion should result in an increase in  $t_0$  with  $x$ . To examine this effect, we performed a least-squares linear fit on  $t_0$ :

$$t_0(x) = a + bx, \quad (4)$$

where  $a = 32.8 \pm 0.6$  ms and  $b = 0.87 \pm 0.4$  s/m. The uncertainties were calculated using error propagation methods. The positive value for  $b$  verifies that the action propagates from left to right and taking the inverse gives a propagation velocity of  $1.15 \pm 0.5$  m/s. This velocity is marginally slower than the velocity calculated by the two electrode pairs in Figure 4 (1.63 m/s) and earlier reports (Carter et al., 2004, 1.5 m/s). Our propagation velocity derived from the optical signal was comparable only to the slowest propagation velocities perhaps because of temporal smearing in our analysis together with the noise contribution which may have blanketed the signal. It could also be due to slower response times for the biophysical components leading to the polarization changes or perhaps the contributions of the smallest, slower axons were greatest (Carter et al., 2004).

## Geometrical Considerations for Signal Sources

In order to identify the source of the polarization signal from the reflection and transmission modes, we analyzed the relative contribution of the signal across the width of the nerve, which correlates to the vertical pixel number. The signal was modeled using Equation 3 and setting  $A_s/A_b = 6.25$ ,  $R_b = 1.67$  mm,  $R_s = 0.42$  mm,  $k_s = 1.76$  mm<sup>-1</sup>, and  $k_b = 0.32$  mm<sup>-1</sup> and fit using means of reduced chi-square ( $\chi^2 = 0.22$  for transmission mode and  $\chi^2 = 2.65$  for reflection mode where  $p > 0.99$ ).

The transmission mode vertical pixel intensity is shown in Figure 7(A). The signal intensity was small near the edges of the nerve and gradually increased to a plateau across the middle of the nerve. A slight decrease in the intensity was observed in the center of the nerve but a paired student's t-test between the circled pixels in Figure 7(A) revealed that this dip was not significant across the 19 nerves recorded ( $p > 0.95$ ). As a result, the simulation (gray dotted line in Figure 7) shows a plateau of intensity across the center of the nerve.

Cohen et al. (1968) found that the signal intensity was larger at the edge of a squid giant axon in transmission mode, hypothesizing that the transmitted polarization signal arises from the edge of an axon. These results, however, originated from a single large axon whereas our data was recorded from a lobster leg nerve which contained bundles of axons surrounded by an outer sheath. While the transmitted signal may peak at the edge of a single axon, a bundle containing hundreds of axons may wash out these peaks revealing an evenly distributed transmitted intensity profile throughout the nerve.

The reflection mode sample data in Figure 7(B) shows significant maxima intensity peaks near the edges of the nerve image ( $p < 0.05$ ). If we assume that the nerve is a uniform cylinder, we expect a symmetric intensity profile, however, the peak intensity at pixel 3 is not as robust as the peak intensity at pixel 16. This discrepancy may be due to the inhomogeneity of the nerves. Furthermore, the light may not have been centered on the nerve resulting in a larger intensity of birefringent light on one side of the nerve relative to the other side of the nerve.

The transmitted signal appears to dominate across the middle of the nerve suggesting that the inner nerve bundle is more transmissive than the outer sheath. Thus, photons traveling through a large portion of the inner nerve bundle material change polarization, but are less likely to scatter at large angles. The peaks appearing at the edge of the nerve in reflection mode imply that more of the signal arises from the fascicle sheath. We conclude that this material is more reflective. The path of a photon on the outer edge of the nerve travels through more outer sheath tissue than a photon elsewhere on the nerve. This longer path length in the fascicle sheath allows for a higher probability that a photon is scattered.

### Action Potential Movie

We compiled the transmission mode spatially resolved images to illustrate the detection of neural activation and action potential propagating along the nerve using polarized light (Figure 8). Beginning at 7.2 ms after the stimulus, sporadic regions on the left end of the nerve begin show a change in polarization which moves right through 10.2 ms. The early components of this response may represent the faster motor axon action potentials. At 10.8 ms, the left portion of the nerve shows activation from the slower axons, mixed with the later parts of the fast action potentials. The signal moves to the right once more at a slower rate, tapering off at 15.6 and 16.2 ms. In these frames, the action potentials appear to propagate from left to right, as would be expected since the stimulus electrodes are on the left side.

In order to compare the propagation velocity determined by the fit data (Figure 5), the nerve image was divided into three regions and the average signal intensity from the outer two regions were used to measure response time. Figure 9 shows the differentiated dI/I signal from regions A and C. The signal from the left region occurs first, verifying that the action potential propagates from left to right. From the rising phase information, the propagation velocity of the action potential volley was calculated to be 2.57 m/s. Our rising phase velocity may reflect the activation of medium axons, whereas the peak response times reported in Figure 6 may be dominated by the slowest axons. While we were able to resolve the slower action potential propagation from the smaller axons, better video technology is required to image the different components comprising the polarization signal, especially the fast rising phase.

### Random Cell Orientation

To test our ability to detect polarization signals within random cell orientations, we tied the nerve in an overhand knot prior to imaging. Our measured EPR signals before and after the imaging window confirm that the action potential propagates through the knotted portion of the nerve. The spatially resolved image of the knot is shown in Figure 10(A). We extracted polarization signals from specific regions in the knotted nerve and fit them to our temporal model (Figure 10B). A decrease in polarized light first occurs in region A, a couple of milliseconds after the stimulus. The dominating signal appears to emanate from the underlying straight portion of the nerve where the orientation of the cells are parallel to the axis of the nerve, as mapped out in Figure 10(C). The signal may be largest from that region of the nerve since the cells are oriented at 45 degrees with respect to the light, the optimal orientation for polarization signals (Cohen et al., 1968; Yao et al., 2005a). The signal in region B shows a later response from region A. Region C physically follows region B and the optical signal in C appears later than the optical signal in B. The latency of the signal in region D shows that the action potential propagates through the entire knot. These experiments confirm that when the sample contains processes with different orientations, the polarization signals are still present and demonstrate the expected latency according to the physical position. Although, the signals are smaller and are observed from specific regions of the nerve where the majority of the fibers are oriented 45 degrees with respect to the light. Presumably, if we had imaged with the polarizers at different angles, different regions of the nerve would have produced a signal.

## Conclusions

Fast optical imaging has the potential to advance brain imaging with higher spatial and temporal resolution than other methods such as EEG or fMRI. Polarization measurements have proven to be advantageous over scattering measurements since cross-polarizers reject many photons unaltered by neural activity (Cohen et al., 1968; Carter et al., 2004). The reduction of the background noise allows for an increase in dynamic range of the imaging system. These increased sensitivity measurements, in turn, increase the signal-to-noise ratio. Further improvements will hinge, in part, on our ability to detect photons that are altered by neural activity and reject those photons not altered by neural activity. Using these techniques in-vivo, however, adds additional complications not present in the lobster nerve such as random orientation of fibers and dendritic, somatic, and glial activation. Random cell orientation hinders the application of these techniques in-vivo; however, our preliminary results using polarization techniques on a knotted lobster nerve support the advantages of using polarized light. When utilizing these imaging techniques in-vivo, we could also make measurements along the polar angles of the Muller matrix to account for random cell orientation (Berezhnyy and Dogariu 2004). By combining the different views and extracting common features in the signal across all angles, we could reduce the noise and characterize the signal more clearly.

## Acknowledgments

This work was supported by NIH MH60263 and grants from the Beckman Young Investigators Fellowship Program, the Murdock Foundation, the Keck Foundation, and the Poncin Foundation.

## References

- Berezhnyy I, Dogariu A. Time-resolved Mueller matrix imaging polarimetry. *Optics Express* 2004;12:4635–4649.
- Carter KM, George JS, Rector DM. Simultaneous birefringence and scattered light measurements reveal anatomical features in isolated crustacean nerve. *J. Neuroscience Methods* 2004;135:9–16.
- Chance B, Luo Q, Nioka S, Alsop DC, Detre JA. Optical investigations of physiology: a study of intrinsic and extrinsic biomedical contrast. *Philos. Trans. R. Soc. Lond. B* 1997;352:707–716. [PubMed: 9232859]
- Cohen LB, Keynes RD, Hille B. Light scattering and birefringence changes during nerve activation. *Nature* 1968;218:438–441. [PubMed: 5649693]
- Cohen LB, Keynes RD, Landowne D. Changes in light scattering that accompany the action potential in squid giant axons: potential-dependent components. *J. Physiol* 1972;224:701–725. [PubMed: 5071934]
- Foust AJ, Beiu RM, Rector DM. Optimized birefringence changes during isolated nerve activation. *Applied Optics* 2005;44:2008–2012. [PubMed: 15835348]
- Foust AJ, Rector DM. Optically teasing apart neural swelling and depolarization. *Neuroscience* 2007;145:887–899. [PubMed: 17303339]
- Furusawa K. The depolarization of a crustacean nerve by stimulation or oxygen want. *J. Physiol* 1929;67:325–342. [PubMed: 16994035]
- Grinvald A. Optical imaging of architecture and function in the living brain sheds new light on cortical mechanisms underlying visual perception. *Brain Topogr* 1992;5:71–75. [PubMed: 1489652]
- Haglund MM, Ojemann GA, Hochman DW. Optical imaging of epileptiform and functional activity in human cerebral cortex. *Nature* 1992;358:668–71. [PubMed: 1495561]
- Hoshi Y, Oda I, Wada Y, Ito Y, Yamashita Y, Oda M, Ohta K, Yamada Y, Tamura M. Visuospatial imagery is a fruitful strategy for the digit span backward task: a study with near-infrared optical tomography. *Cognitive Brain Research* 2000;9:339–342. [PubMed: 10808144]
- Landowne D. Molecular motion underlying activation and inactivation of sodium channels in squid giant axons. *J. Membrane Biol* 1985;88:173–185. [PubMed: 2419567]
- Rector DM, Ranken DM, George JS. High-performance confocal system for microscopic or endoscopic applications. *Methods* 2003;30:16–27. [PubMed: 12695100]

- Rector DM, Carter KM, Volegov PL, George JS. Spatio-temporal mapping of rat whisker barrels with fast scattered light signals. *NeuroImage* 2005;26:619–627. [PubMed: 15907319]
- Tasaki I, Byrne PM. The origin of rapid changes in birefringence, light scattering and dye absorbance associated with excitation of nerve fibers. *Japanese Journal of Physiology* 1993;43:S67–S75. [PubMed: 7505858]
- Uma Maheswari RU, Takaoka H, Kadono H, Homma R, Tanifuji M. Novel functional imaging technique from brain surface with optical coherence tomography enabling visualization of depth resolved functional structure in vivo. *Journal of Neuroscience Methods* 2003;124:83–92. [PubMed: 12648767]
- Yao XC, Foust A, Rector DM, Barrowes B, George JS. Cross-polarized reflected light measurement of fast optical responses associated with neural activation. *Biophysical Journal* 2005a;88:4170–4177. [PubMed: 15805175]
- Yao XC, Yamauchi A, Perry B, George JS. Rapid optical coherence tomography and recording functional scattering changes from activated frog retina. *Appl Opt* 2005b;44(11):2019–2023. [PubMed: 15835350]

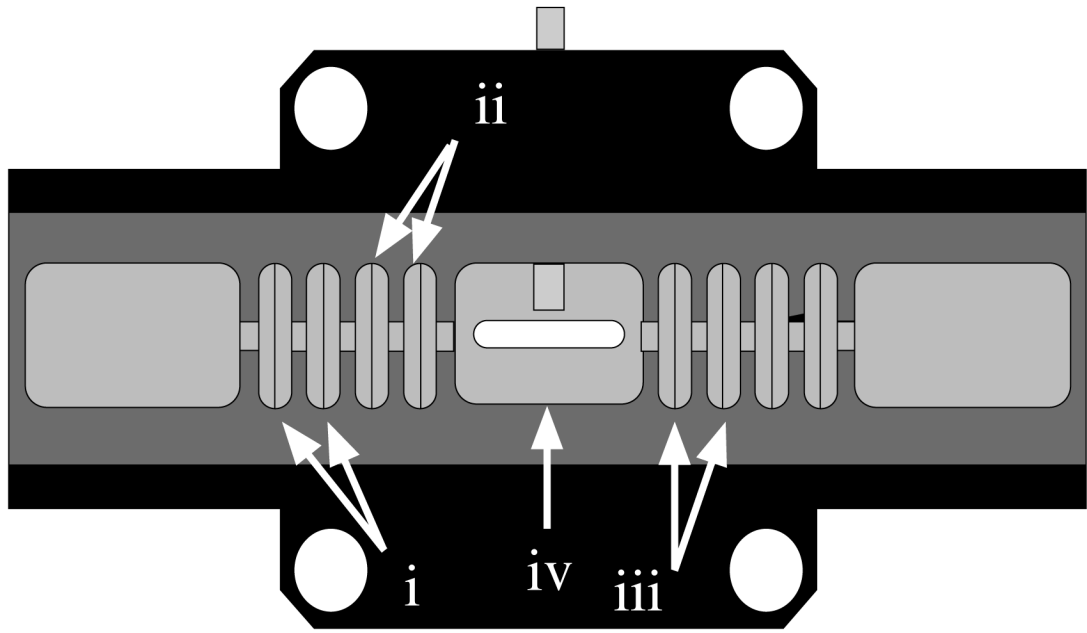


**Figure 1.** Lobster nerve chamber. Stimulating current was delivered by a pair of electrodes (i). The electrophysiological response (EPR) from summed population action potentials was recorded pre-optical (ii) and post-optical (iii). Polarized light shone onto the nerve through the imaging window (iv).

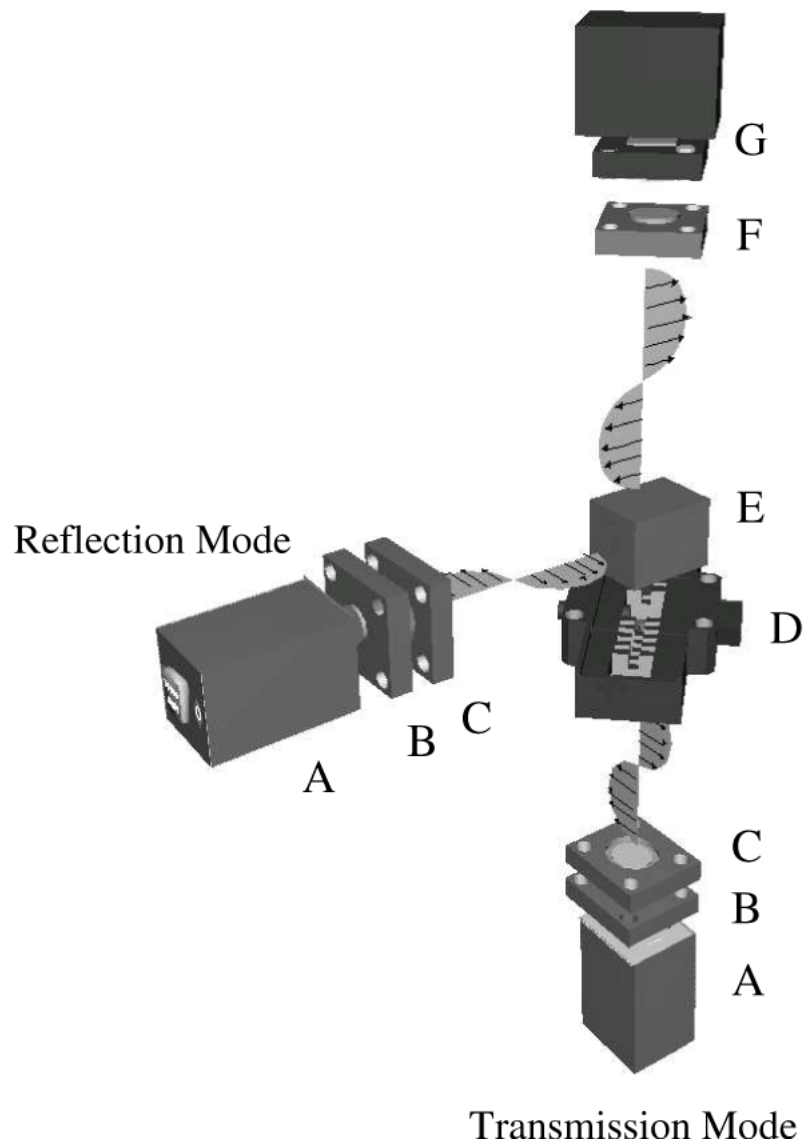


**Figure 2.** Schematic diagram of the transmission mode experimental system (starting from the bottom). Light in the near-infrared spectrum emitted by an SLD (A) was collimated by a lens ( $f = 5$  mm) (B) and polarized 45 degrees with respect to the nerve (C). The light passed through the imaging window of the lobster sample chamber (D). Polarized light from the nerve passed through a second polarizer (E). The image was focused by a second lens ( $f = 12.5$  mm) (F) and images were collected by a CCD camera (G). In reflection mode (starting from the left), near-infrared light emitted by an SLD (A) was collimated by a lens ( $f = 5$  mm) (B). The light passed through a polarizer (C), which only transmitted *s*-polarized light. The *s*-polarized light was reflected by a polarizing beamsplitter (for reflection mode, the polarizer was replaced by a polarizing beamsplitter) (E) onto the nerve (D). Scattered light from the nerve traveled back through the polarizing beamsplitter, which only transmitted *p*-polarized light. The light was focused by a lens ( $f = 12.5$  mm) (F) onto a CCD camera (G).

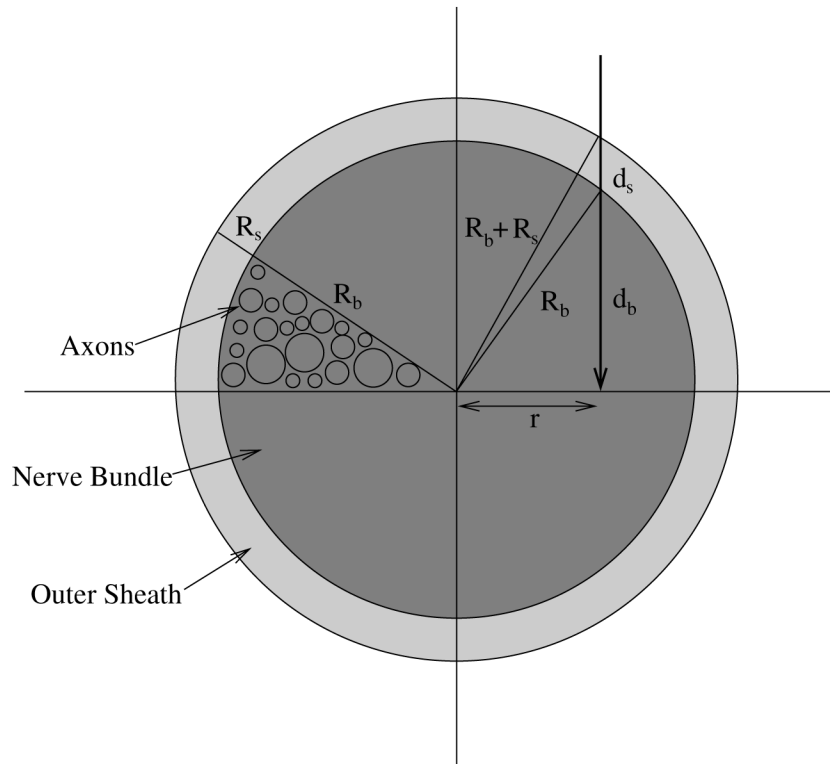


**Figure 3.**

The nerve was modeled as a cylindrical nerve bundle of radius  $R_b$  encased by a membrane of thickness  $R_s$ . A light ray, indicated by the arrow, displaced by a distance  $r$  from the center of the nerve traveled a distance  $d_s$  and  $d_b$  through the membrane and bundle, respectively.

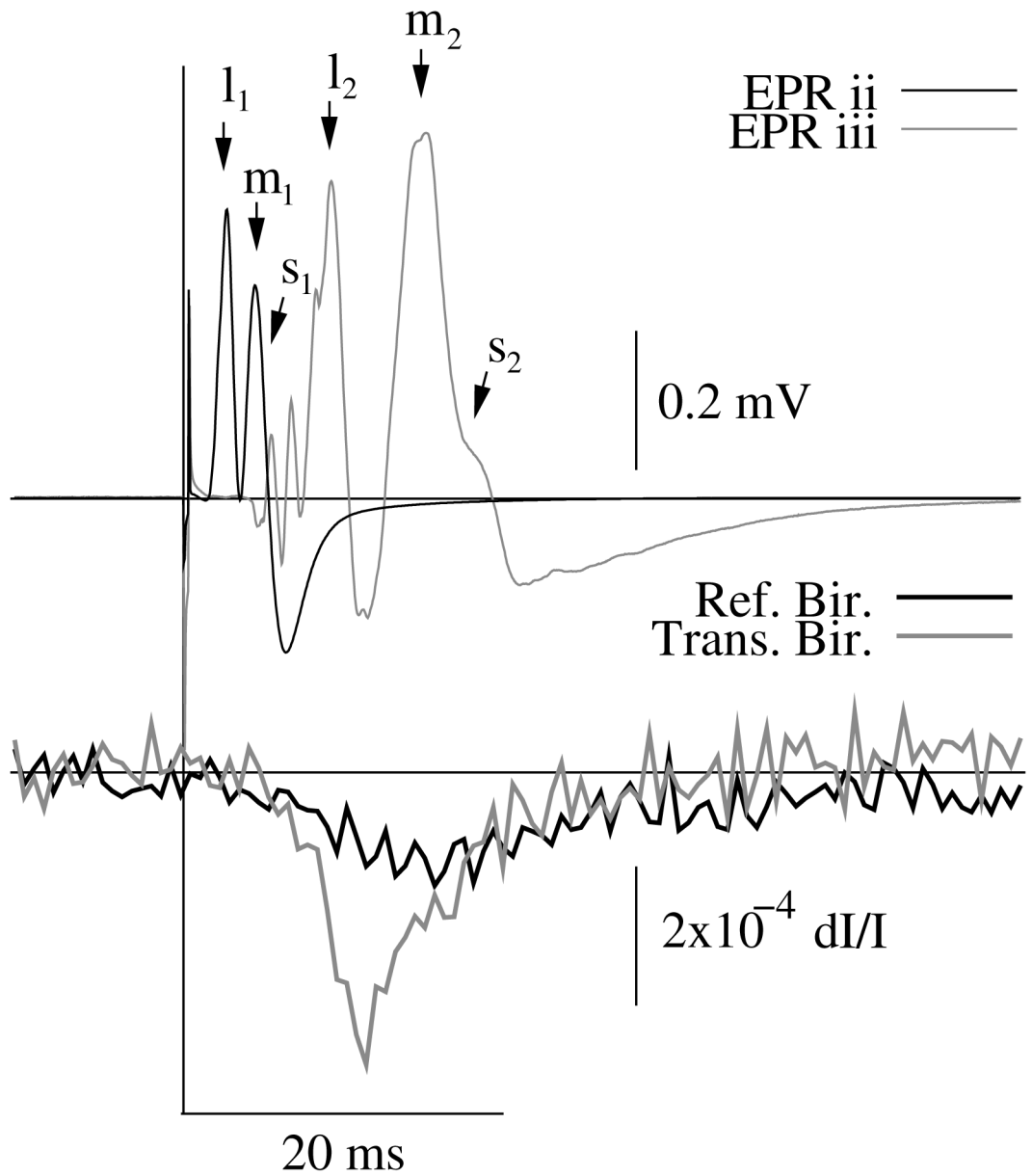


**Figure 4.**

Electrical and optical measurements of a lobster nerve. The vertical line indicates the time of stimulus. The upper panel shows the EPR before the imaging window (thin black trace) and after the imaging window (thin gray trace). The action potential contains multiple components corresponding to axons with different diameters. Signal components from EPR ii are labeled as large ( $l_1$ ), medium ( $m_1$ ), and small ( $s_1$ ) axons and signal components from EPR iii are labeled as large ( $l_2$ ), medium ( $m_2$ ), and small ( $s_2$ ) axons. The optical signal was obtained by averaging all of the pixels in the CCD array and dividing the change in intensity by the baseline intensity. The thick black trace is the transmitted signal and the thick gray trace is the reflected signal.

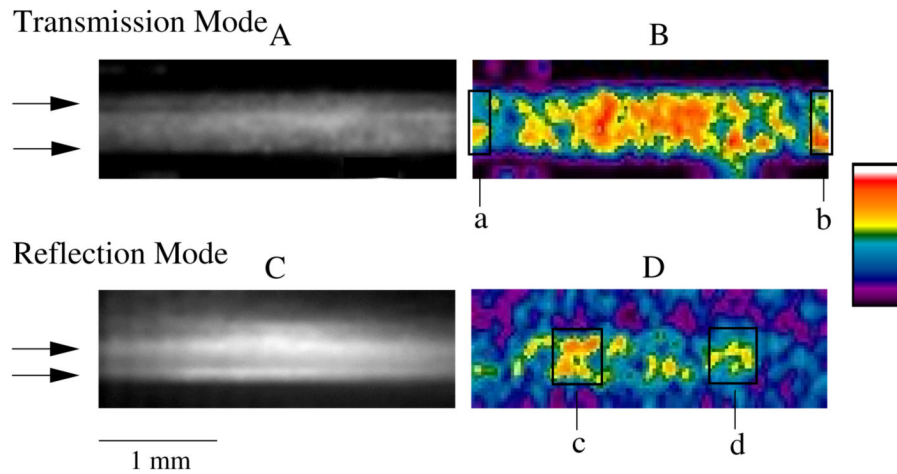


**Figure 5.**

An image of the transmission mode intensity averaged over time is displayed in (A). The arrows indicate the edge of the nerve. The pseudo-colored amplitude image of the transmission mode baseline corrected signal summed from 18 ms to 55 ms for each pixel is shown in (B). Decreases in polarized light correspond to warm colors where black pixels represents 0 dI/I and white pixels represent  $2 \times 10^{-3}$  dI/I. The signal intensity is evenly spread throughout the nerve. An image of reflection mode intensity is displayed in (C). The arrows indicate the edges of the fascicle. The reflection mode pseudo-colored amplitude image is shown in (D) where a decrease in polarized light corresponds to warmer colors with black pixels representing 0 dI/I and white pixels representing  $1 \times 10^{-3}$  dI/I. The regions of maximum amplitude are mostly located near the fascicle edges. The signals in regions a, b, c, and d were averaged together and fit to the temporal model shown in Figure 6.

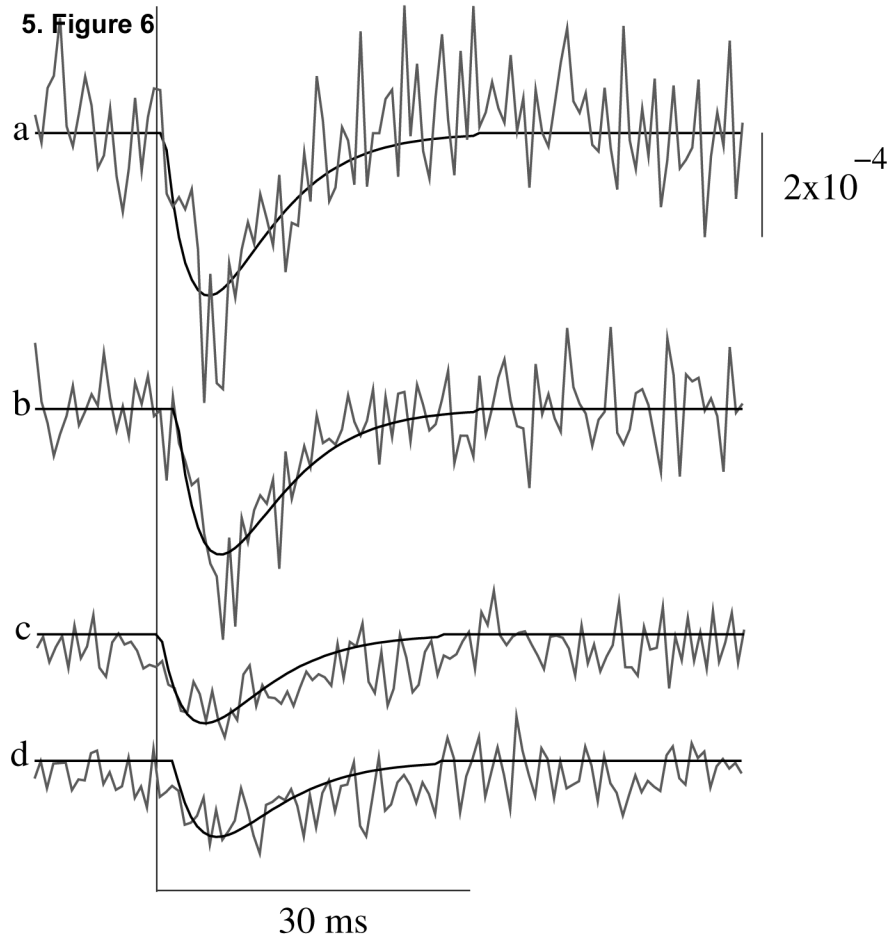


**Figure 6.**

Plot of the light intensity changes as a function of time, for four regions (shown in Figure 5); two in transmission mode (a and b) and two in reflection mode (c and d). The solid black line is a fit to the data (gray line) using Eq. (4). A least squares fit of the temporal model across the length of the nerve showed that the action potential propagates from left to right with a velocity of  $1.15 \pm 0.5$  m/s.

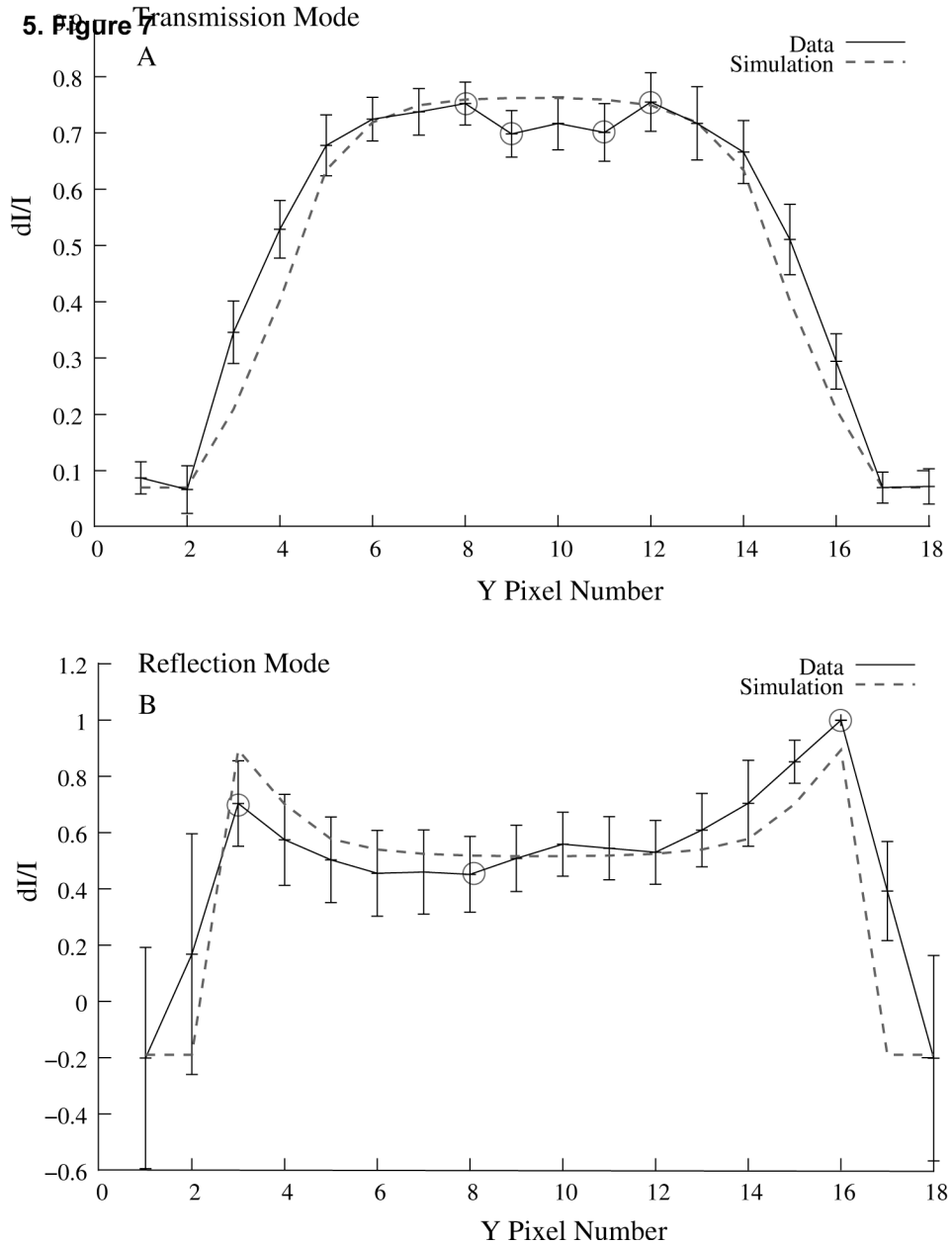


**Figure 7.**

Panel (A) illustrates a plot of the transmission mode signal amplitude as a function of distance ( $Y$ ), obtained by averaging pixels horizontally, along the length of the nerve. The sample data is the signal of 19 nerves stretched to a set size, normalized to one, and then averaged together. The dashed line was obtained by means of best fit using Eq. (7). The intensity is small along the edges of the nerve and gradually increases towards the middle. A paired student's t-test shows that differences between the highest and lowest points in the middle (circled) are insignificant even at 14 degrees of freedom and a 95% confidence interval (pixel 8 versus pixel 9,  $t=2.13$ ; pixel 11 versus pixel 12,  $t=1.34$ ). Overall, the signal is evenly distributed throughout the middle of the nerve. Panel (B) shows a plot of the reflection mode scattering amplitude as a function of distance ( $Y$ ) where the two peaks that correspond to maxima in the signal occur at the edges of the fascicle. A paired student's t-test confirms that the signal intensity between

the edge and center of the nerve (circled) is significant at 3 degrees of freedom and a 95% confidence level (pixel 3 versus 8,  $t = 4.88$ ; pixel 8 versus pixel 16,  $t = 4.05$ ). The dashed line is a fit to the data using Eq. (8). The data was averaged from 3 nerves, each stretched to a set size to account for width variations and then the intensity is normalized to one.

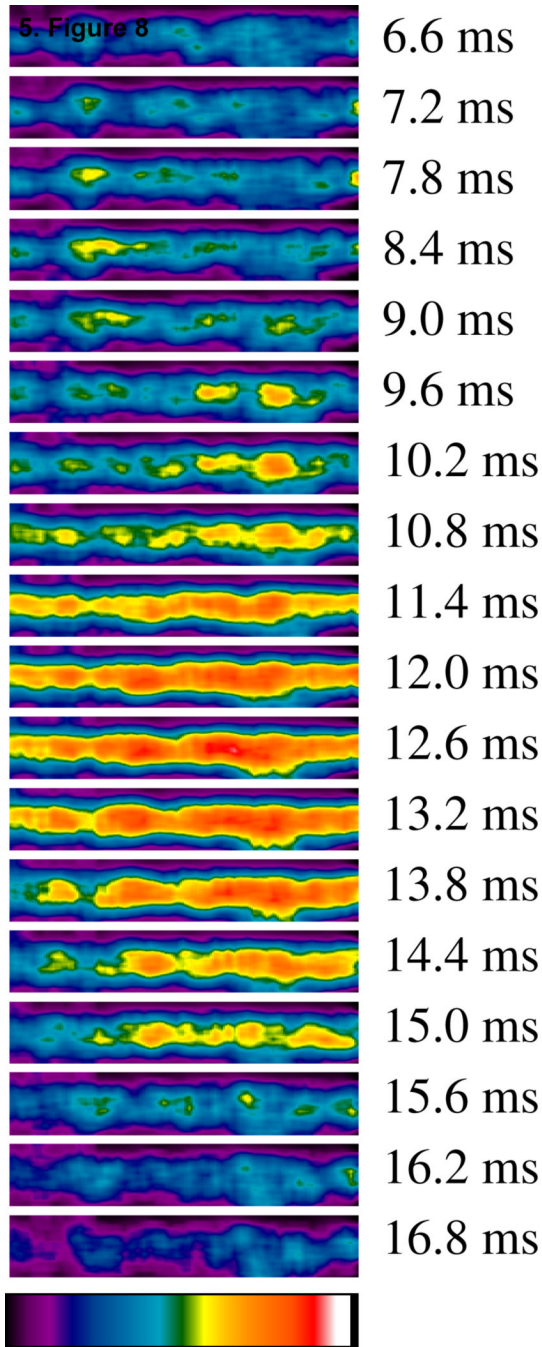


**Figure 8.**

Transmission mode action potential movie. Each frame was subtracted from the baseline intensity and divided by the DC light intensity resulting in  $dI/I$ . A decrease in intensity corresponds to warmer colors where black pixels are equivalent to 0  $dI/I$  and white pixels are equivalent to  $1 \times 10^{-4}$   $dI/I$ . The time is in milliseconds after the stimulus. Neural activation begins at 7.2 ms on the left side of the image and peak activation occurs at 12.6 ms. Between 7.2 ms and 10.2 ms, an early propagation is seen from left to right which may represent action potentials from the larger/faster axons. Action potentials again propagate from left to right, but slower from 10.8 ms to 16.2 ms, as is seen by the slower decay of the signal on the right side of the nerve, possible representing action potentials from smaller/slower axons.

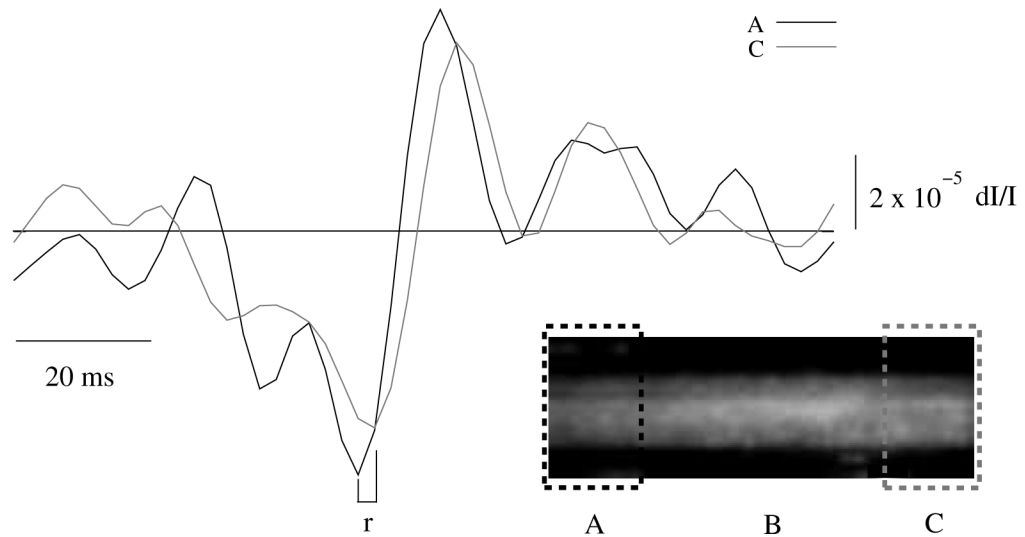


**Figure 9.**

The nerve image shown in the upper panel was divided into three regions, A, B, and C with the middle region (B) twice the size of the outer two regions (A, C). The black line represents the leftmost region (A) and the gray line represents the rightmost region (C). The differentiated optical response was plotted for the leftmost region and the rightmost region. The left region leads the response verifying that the action potential propagates from left to right. The propagation velocity was calculated to be 2.57 m/s for the rising phase (r).

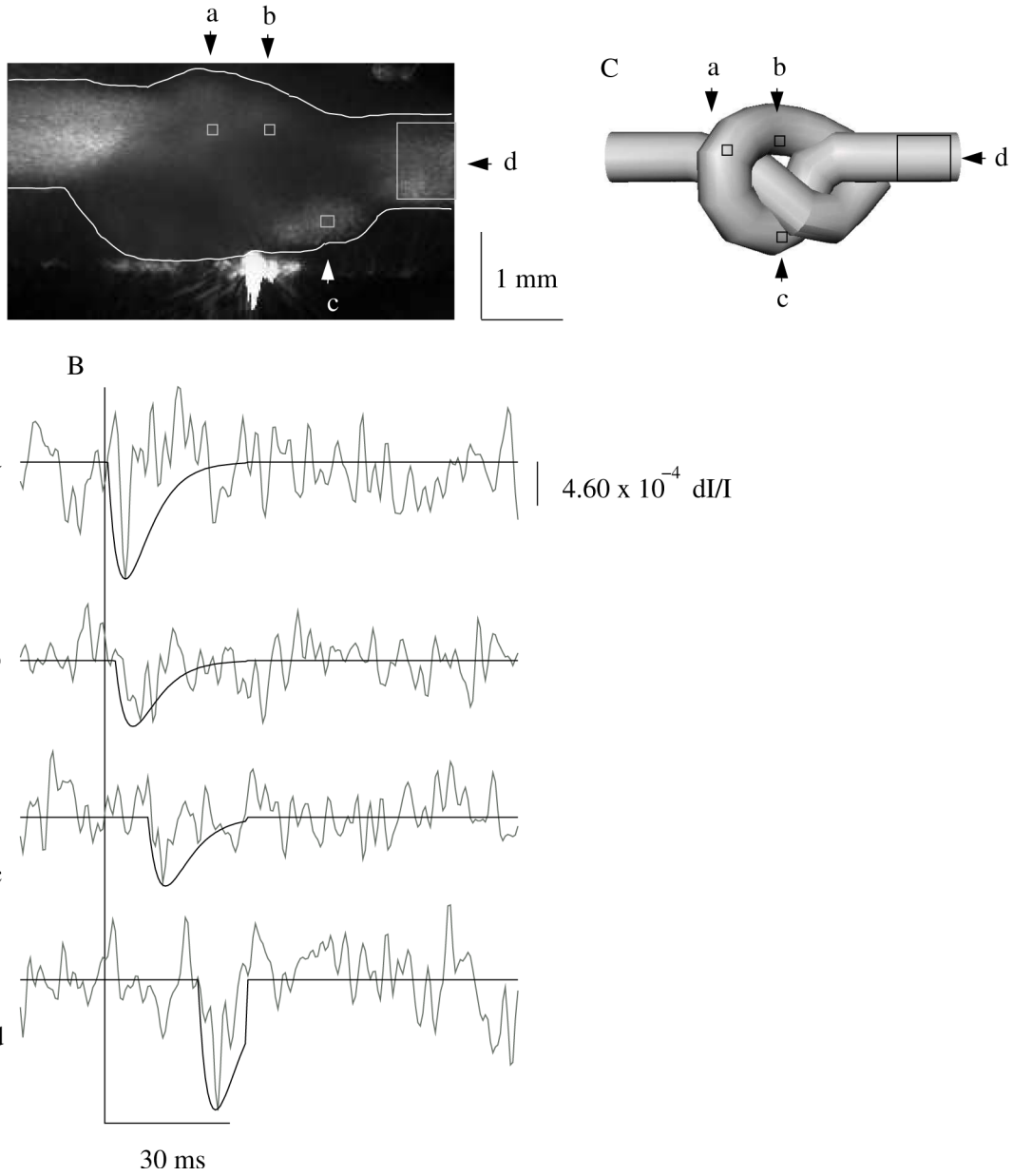


**Figure 10.** Panel (A) is an image of the transmitted light averaged over time with the nerve tied in an overhand knot. The solid black lines in (B) are fit to the raw data, shown in gray, using Eq. 2. The time component confirms that the action potential first passes through pixel a, then through pixel b, following in pixel c and finally through pixel d which is the expected course of the action potential according to the geometry of the knot as mapped out in (C).